scientific reports

Check for updates

OPEN

Impact of plasma discharge pressure on implant surface properties and osteoblast activities in vacuum-assisted plasma treatment

Ara Jung[1,2,7], Hyungyu Lee[3,4,7], Heejin Kim[1,2], Hyun Jeong Jeon[5], Sanghoo Park[6]✉ & Bomi Gweon[1]✉

Nonthermal plasma has been extensively utilized in various biomedical fields, including surface engineering of medical implants to enhance their biocompatibility and osseointegration. To ensure robustness and cost effectiveness for commercial viability, stable and effective plasma is required, which can be achieved by reducing gas pressure in a controlled volume. Here, we explored the impact of reduced gas pressure on plasma properties, surface characteristics of plasma-treated implants, and subsequent biological outcomes. Implant materials were treated with plasmas under varying discharge conditions, with pre-pumping times of 10 s and 20 s, thereby modulating the pressure during plasma treatments. Through optical emission spectroscopy, we demonstrated that the 5 Torr operational condition, achieved by 20-s pre-pumping, generated a greater density of excited nitrogen species and provided more stable plasma compared to the 16 Torr condition, achieved by 10-s pre-pumping. We then assessed the surface hydrophilicity, chemical composition, protein adsorption, and osteoblast activities on plasma-treated implants compared with those of untreated controls. Our results reveal that the 5 Torr condition significantly enhances removal of carbon-based impurities and increased protein adsorption, leading to improved cell adhesion, proliferation, and differentiation. In particular, implants treated under the 5 Torr condition showed significantly higher carbon-based impurity reduction and osteoblast differentiation performance compared to those treated under the 16 Torr condition. These findings suggest that optimizing gas pressure in plasma devices is critical for effectively controlling excited nitrogen radicals, which improves plasma surface modification and enhances the biocompatibility of implant surfaces.

Keywords Vacuum plasma, Plasma treatment, Plasma cleaning, Osteointegration, Surface wettability

Low-temperature plasma has been extensively utilized in various biomedical fields due to its reactive species, including electron, ions, radicals, and photons, which readily react with molecules or break chemical bonds in substrates it encounters. Its applications range from surface modification[1–3] and sterilization[4–7] to wound healing[8,9] and cancer treatment[10–13]. Notably, low-temperature plasma is particularly advantageous in surface engineering, as plasma-assisted dry etching methods are superior to traditional wet etching methods[14–16].

For medical implants, such as those used in dental or orthopedic applications, surface modification is crucial because the characteristics of the implant surface significantly impact its performance. Key surface characteristics, including chemical composition, surface energy (or wettability), cleanliness, and topography, can affect biocompatibility, cellular activities, and osseointegration[17–20]. In particular, to enhance the surface energy and

[1]Department of Mechanical Engineering, Sejong University, Seoul, Republic of Korea. [2]Department of Biomedicine & Health Science, College of Medicine, The Catholic University, Seoul, Republic of Korea. [3]Institute of Mechanical Technology, Korea Advanced Institute of Science and Technology (KAIST), Daejeon, Republic of Korea. [4]Department of Electrical and Biological Physics, Kwangwoon University, Seoul, Republic of Korea. [5]Plasmapp Co., Ltd, Yongin-si, Gyeonggi-do, Republic of Korea. [6]Department of Nuclear and Quantum Engineering, Korea Advanced Institute of Science and Technology (KAIST), Daejeon, Republic of Korea. [7]Ara Jung and Hyungyu Lee contributed equally to this work. ✉email: sanghoopark@kaist.ac.kr; bgweon@sejong.ac.kr

cleanliness of implants, various techniques, such as plasma and ultraviolet (UV) treatment, have been introduced. Both methods effectively remove impurities by delivering sufficient energy to dissociate the hydrophobic organic substances including hydrocarbons from the implant surface[20–25]. In plasma treatment, high-energy electrons, ions, radicals, and UV photons contribute to breaking molecular bonds in impurities, facilitating their removal[1,26–28]. In UV treatment relies mainly on UV photos to achieve a similar outcome[20,29,30]. These processes enhances surface wettability, which subsequently promotes cellular activities and osseointegration[20–24]. While treatment outcomes may vary depending on the specific treatment conditions, several studies have shown that plasma treatment is more effective in enhancing surface wettability and promoting cell proliferation compared to UV treatment[31–33].

Based on these benefits, plasma treatment is recognized as a highly promising method among various surface modification methods[2,34–37]. In particular, atmospheric pressure plasma offers the advantage of producing numerous reactive species with high number densities, which effectively remove impurities and form functional groups on the surface, thereby improving protein adsorption and cell adhesion[24,38,39]. However, such collisional plasmas generated in air at ambient pressure have short characteristics length and time scales, resulting in a limited plasma volume. This negatively impacts plasma uniformity and limits the effect of the plasma to small regions. Moreover, because the plasma characteristics are strongly affected by the condition of the ambient air, such as the relative humidity and temperature, achieving consistent results is challenging. To overcome these issues, supplying noble gases such as argon or helium are often conducted to generate a stable and volumetric plasma. However, these gases require costly and cumbersome gas cylinders, which are impractical for widespread use.

To address these limitations, plasma treatment devices operated at reduced gas pressures have been suggested for implant surface treatment. In our previous studies, we demonstrated that a vacuum-assisted dielectric barrier discharge (DBD) effectively modifies the implant surface and improve osteoblast activity[1]. Nevins et al. evaluated the efficacy of plasma treatment at a base pressure of approximately 5 Torr on titanium implant materials. Their results indicated that plasma-treated implants had significantly higher bone-to-implant contact (BIC) than control implants in canines, suggesting the potential of plasma treatment in improving implant performance[22].

Despite recent advancements in plasma treatment for dental implants, the link between plasma discharge conditions, the radicals generated within plasmas, and the resulting biological outcomes is not yet completely understood. These biological outcomes include the interactions of proteins and cells with the implant surface as well as the interactions between bone tissues and the implant surface. To fill this gap in knowledge, we comprehensively investigated the effects of different plasma discharge conditions on dental implant surfaces. By varying the plasma discharge conditions, specifically by changing the gas pumping time to adjust the operating pressure, we aimed to establish a correlation between these conditions and the observed biological outcomes. We assessed the efficiency of surface modification by measuring surface wettability and impurity content and subsequently quantified osteoblast cell activities. Our findings provide insights that can guide the optimization of plasma treatment to enhance implant performance.

Experimental methods

Plasma module setup

Our plasma module comprises two electrodes, an implant, a fixture driver and holder, and a quartz tube. This configuration was based on an implant surface treatment device, the ACTILINK system (Plasmapp Co., Ltd). As depicted in Fig. 1A, the implant, fixture driver and its holder, and base plate electrode are all in electrically contact and grounded. A high-voltage power supply (Plasmapp Co., Ltd) was used to apply a 100 kHz sinusoidal electric power with a voltage of 3 kVpp to the top electrode to initiate plasma generation between the top electrode and the implant surface.

The quartz tube, with a diameter of 32 mm and a height of 140 mm, functions as a vacuum chamber that can withstand low vacuum. As illustrated in Fig. 1A, the fixture driver is specifically designed to establish a connection with the implant, and its opposite end is linked to the driver holder. To remove gas from the quartz-enclosed chamber, a diaphragm vacuum pump (N 84.3 ANDC, KNF) is attached to the module via a 6 mm pipe, with a pressure gauge installed to monitor the pressure level. As shown in Fig. 1B, a silicone stopper is placed at the bottom of the quartz tube to prevent air leakage; therefore, the pressure within the quartz chamber was consistently maintained within the range of 3 to 5 Torr after pumping.

As shown in Fig. 1C and D, following a 10-second pre-pumping period (will be denoted as 10s-pumping), the area covered by plasma expanded gradually over time, whereas in the case of a 20-second pre-pumping period (will be denoted as 20s-pumping), the coverage area remained relatively consistent. Another notable difference observed in the discharge images was the presence of striations within the positive column. Specifically, the 20s-pumping case exhibited clearer striations.

These striations arise from fluctuations in electron and ion densities, which are related to pressure variations. As the pressure steadily decreased during the plasma discharge in the 10s-pumping case, the clarity of striations within the positive column diminished accordingly.

In this study, a commercial implant (SLA, #SFR4008NS, Hoowon) with a diameter of 4.0 mm and a length of 8.5 mm was employed. Plasma treatment was conducted for 10 s after either a 10s- or 20s-pumping period to evaluate the impact of discharge pressure on the outcome of the implant surface treatment. The graph presented in Fig. 2 shows the temporal pressure profile within the quartz chamber. Upon commencement of pumping, the pressure decreases exponentially over time. At 10 s and 20 s after the initiation of pumping, the pressures were measured to be approximately 16 Torr and 5 Torr, respectively, as indicated by the red arrowheads in regions A and B of Fig. 2. This graph shows a continuous pressure decline during the discharge following the 10s-pumping, while the pressure remains stable during the discharge following the 20s-pumping. For clarity regarding the

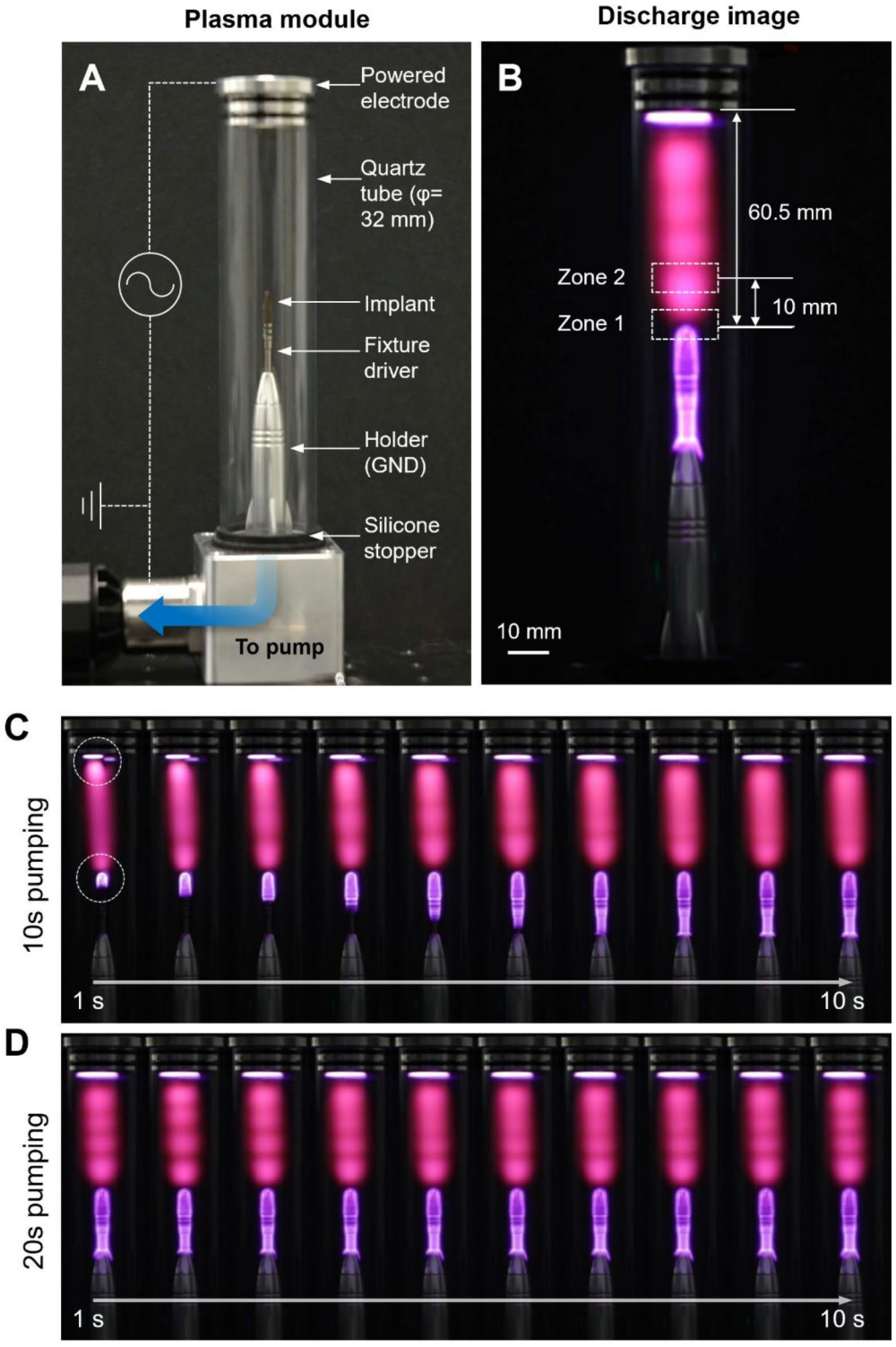

Fig. 1. (**A**) The image of plasma module and its configuration. (**B**) Plasma discharge image showing the defined zones (zone 1 and zone 2) in the discharge column. Sequential images of plasma discharge taken at 1-second intervals after (**C**) 10-second pre-pumping and (**D**) 20-second pre-pumping.

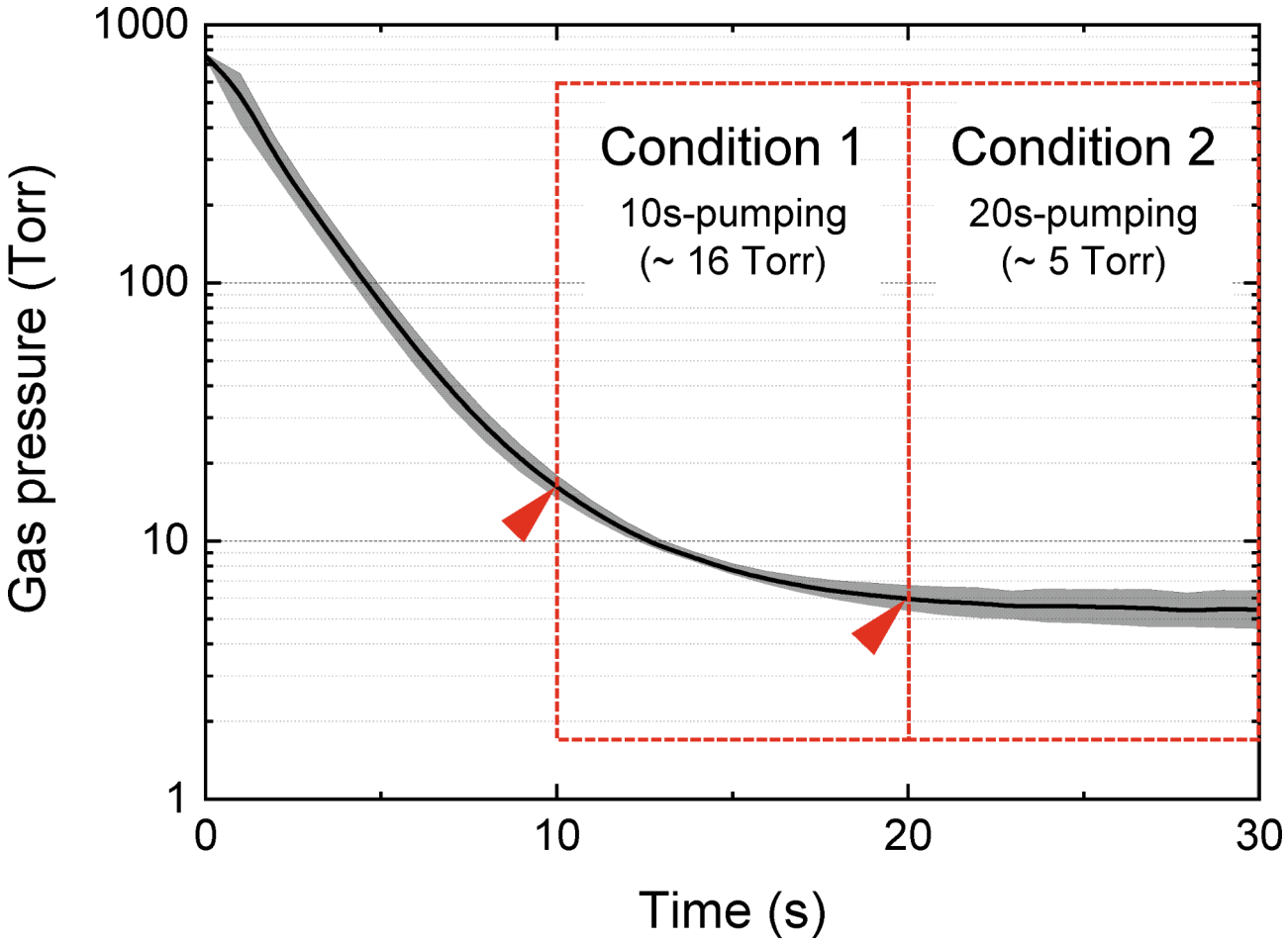

Fig. 2. Temporal profile of the gas pressure inside the plasma module. Initial pressure of experimental Condition 1 (10s-pumping) is approximately 16 Torr and Condition 2 (20s-pumping) is approximately 5 Torr, as indicated by the red arrowheads. Data is shown as mean ± s.d. (n= 8).

plasma conditions, the 10s-pumping and 20s-pumping conditions will hereafter be referred to as the '16 Torr' and '5 Torr' conditions, respectively.

Spectroscopy setup

Plasma emission spectra were acquired utilizing two different spectroscopic setups: a UV-visible spectrometer (OceanOptics Maya2000 Pro) and a monochromator (Dongwoo MonoRa 500i) equipped with an ICCD camera (Andor iStar 340T). The emitted light from the plasma was transmitted through an optical fiber (Ocean Optics QP400-2-SR), which was connected to a collimating lens adapter (Ocean Optics 74-UV). The UV-visible spectrometer measured a broad emission spectrum ranging from 200 to 1100 nm, while the monochromator and ICCD camera pair captured high spectral resolution spectra, specifically targeting the N_2^+ first negative system (388–392 nm) and the N_2 second positive system (310–400 nm). Each spectrum was obtained to investigate the temporal characteristics of the emission spectrum with an integration time of 1 s. Plasma emission spectra were measured at two distinct positions, denoted by zone 1 and zone 2, as illustrated in Fig. 1B. Zone 1 corresponds to the plasma at the implant surface, while zone 2 corresponds to the plasma 10 mm away from the implant surface. The spectrum obtained from zone 1 primarily reflects emissions from the plasma sheath, while the spectrum acquired from zone 2 shows emissions from the bulk plasma.

Photography setup

In addition to the emission spectra, plasma discharge images were captured using a digital single-lens reflex (DSLR) camera (Canon EOS 500D). The images shown in Fig. 1C and D were taken with a 0.5-s exposure time and an International Standardization Organization (ISO) setting of 250. Sequential images were captured at 1-s intervals for a total of 10 s to monitor the changes in plasma discharge and emission light over time.

Assessing the characteristics of the implant surface using XPS

To characterize the chemical composition of the implant surface, X-ray photoelectron spectroscopy (XPS) was performed using an X-ray photoelectron spectrometer system (ULVACPHI INC, PHI 5000 VersaProbe III). The analysis primarily focused on the levels of carbon-based impurities and oxygen on the implant surfaces.

The atomic concentrations of carbon and oxygen on the surfaces of the control implant and the plasma-treated implants (with pumping time of 10–20 s, and plasma treatment time of 10 s) were analyzed and compared. Each measurement was repeated three times.

Protein adsorption assay

Following plasma treatment, the control implants and plasma-treated implants were submerged in a 96-well plate containing fibronectin solution (50 µg/ml, #356008, Corning) and incubated at 37 °C for 2 h. The implants were then rinsed with phosphate-buffered saline (PBS) to remove nonadsorbed fibronectin proteins from the surface. Adsorbed fibronectin proteins on the implant surfaces were lysed using a 2% sodium dodecyl sulfate (SDS) solution at 37 °C for 18 h. The amount of fibronectin in the lysate was then measured using a Micro BCA™ protein assay reagent kit (#23235, Thermo Fisher Scientific).

Quantification of cell proliferation

To investigate whether plasma treatment improves osteogenesis, an osteoblast-like cell line, Saos-2, was used for in vitro experiments[20,40]. Saos-2 cells were purchased from the Korean Cell Line Bank (#80023, KCBL) and cultured with minimum essential medium (#LM007-01, Welgene) supplemented with 10% fetal bovine serum (FBS, #S001-01, Sigma) and 1% antibiotic-antimycotic (Anti-Anti #CA002-010, GenDEPOT). To mimic the bone implantation environment, a high concentration of osteoblasts was prepared in cell suspensions. Following plasma treatment, the control and plasma-treated implants were submerged in a 96-well plate containing a Saos-2 cell suspension (1×10^6 cells/well) and incubated in a CO_2 incubator for 2 h to allow the cells to adhere to the implant surface. After incubation, the implants were removed from the cell suspension, gently rinsed with PBS to remove nonadherent cells, and transferred to a new 96-well plate containing fresh cell culture medium. The number of viable cells adhered to the implant surfaces within 2 h was quantified using a Cell Counting Kit-8 (CCK-8, #CK04, Dojindo). Subsequently, cell proliferation was assessed with the CCK-8 assay at day 1 and day 7. The experimental timeline is shown in Figure S1. For the CCK-8 assay, the implants were transferred to a 96-well plate containing fresh cell culture medium supplemented with 10% CCK-8 reagent at each time point. The implants were then incubated for 90 min to allow the cells on the implant surface to react with the CCK-8 reagent. After 90 min, the optical density (OD) value was measured at a wavelength of 450 nm using a microplate reader (AMR-100, Allsheng). Each measurement was repeated five times.

Quantification of cell differentiation

To measure the differentiation of osteoblasts, we assessed the activity of alkaline phosphatase (ALP), a differentiation marker for osteoblasts, using an ALP test kit (#ab83369, Abcam)[21,41]. We followed the same procedure used in the cell proliferation process to attach cells to the implant surface and allow them to proliferate and differentiate. The control and plasma-treated implants were submerged in a 96-well plate containing a Saos-2 cell suspension at a concentration of 1×10^6 cells/well and incubated in a CO_2 incubator for 2 h. After 2 h of incubation, nonadherent cells were rinsed out with PBS, and the implants were transferred to a 96-well plate containing fresh cell culture medium. The cells were then cultivated on the implants for 7 days. The experimental process and timeline leading up to the ALP measurement is shown in Figure S1. After 7 days, the implants were placed in ALP buffer on ice for 30 min to lyse the cells. The cell lysate was centrifuged at 13,000 rpm and 4 °C for 15 min to remove cell debris. Subsequently, 80 µl of lysate and 50 µl of a 5 mM p-nitrophenyl phosphate (pNPP) solution were mixed in a 96-well plate and incubated at 25 °C for 60 min in the dark. A stop solution was added to halt the reaction. The OD was determined at a wavelength of 405 nm using a microplate reader (AMR-100, Allsheng). The ALP activity was quantified using a pNPP standard curve.

Immunofluorescence staining

To image cells attached to the implants, we fixed and fluorescently labeled the cells[42]. We followed the same procedure used in the cell proliferation process to attach cells to the implant surface and allow them to proliferate (Figure S1). After 7 days of incubation in cell culture media, the implants with adhered cells were washed with PBS and fixed in a 3.7% formaldehyde solution. Following fixation, the cells were permeabilized with 0.2% Triton X-100 solution for 10 min. The implants were then labeled with rhodamine phalloidine (Invitrogen, #R415) to stain actin and with Hoechst 33,342 (Invitrogen, #H1399) to stain the nucleus. The cells were imaged using a fluorescence microscope (Leica DMI8) at magnifications of 5× and 10×.

Results and discussion

Plasma emission spectrum

To investigate the difference between the plasmas under the 16 Torr and the 5 Torr, we conducted optical emission spectroscopy (OES). First, to gain a preliminary understanding of the overall species in the emission spectra, we used a spectrometer capable of capturing broadband spectra ranging from 200 to 1100 nm. As expected from the common air-based discharges, N_2 molecular spectra were dominant. The full spectrum of plasma emission from zone 1, which encompasses emissions from the N_2 second positive system, the N_2^+ first negative system, and the O atom emission peak at 777 nm, is shown in Figure S2. Compared with the 5 Torr case, the maximum intensity observed in the 16 Torr case was approximately three times higher and exhibited a swifter rate of decrease over time (Figure S2).

Next, to investigate the detailed changes in the emission spectrum of interest, we acquired optical emission spectra using the monochromator and ICCD camera pair. Figure 3 shows the emission spectrum from zone 1. Consistent with the trend described above (Figure S2), the peak intensity in the 16 Torr case was greater than that in the 5 Torr case, and the intensity progressively declined over time. The measured spectra provide detailed information on the emissions from the N_2 second positive system and N_2^+ first negative system. Under

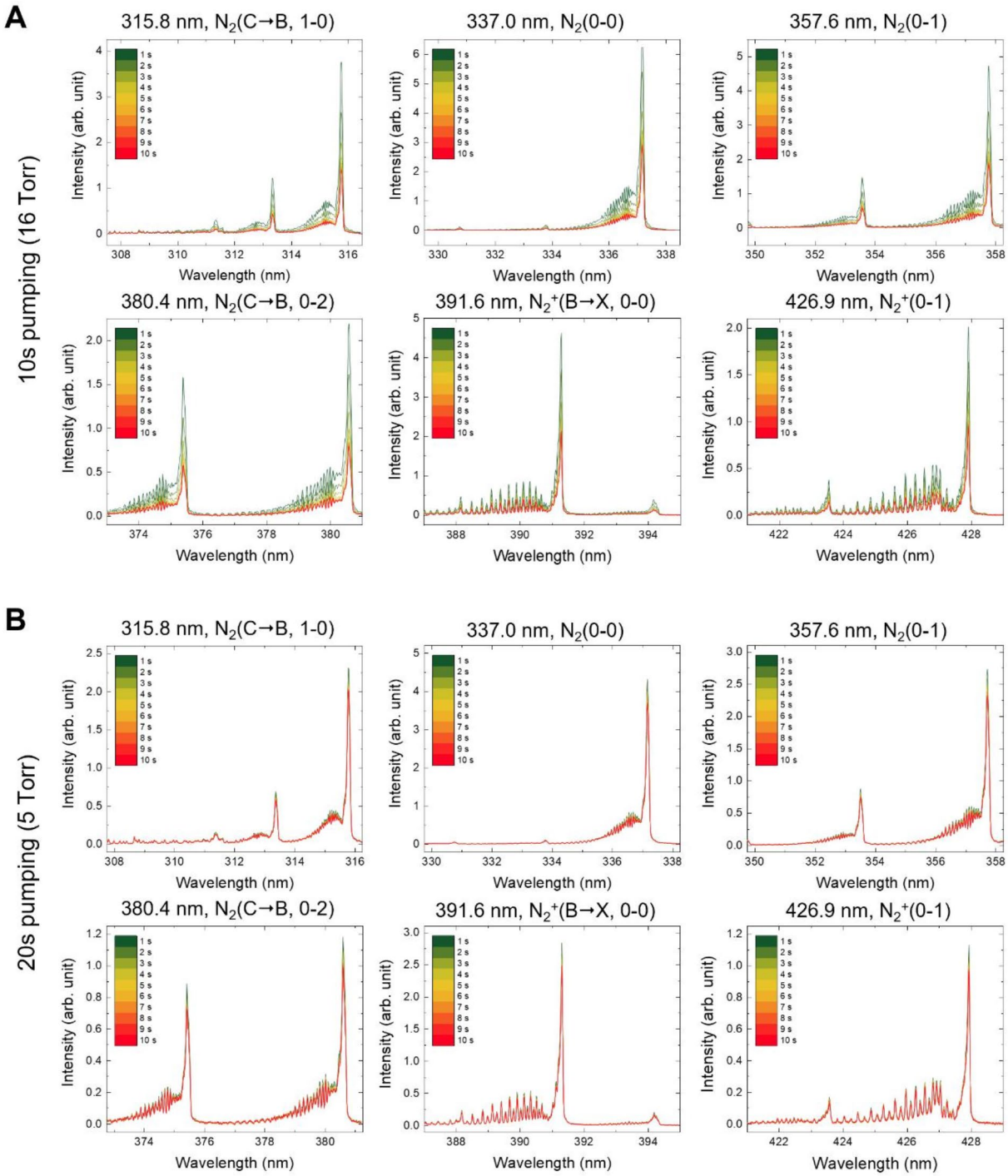

Fig. 3. Plasma emission spectrum from zone 1 at different wavelength during plasma discharge after (**A**) 10 s of pumping (16 Torr), and (**B**) 20 s of pumping (5 Torr).

the 16 Torr condition, the peak intensity decreased by approximately 50% over 10 s. However, the changes in intensity distribution within the rotational structure of the spectrum were relatively insignificant. Conversely, the decrease in peak intensity was less pronounced under the 5 Torr condition, and there was almost no change in intensity distribution within the rotational structure of the spectrum.

To compare the spectra emitted from the plasma at the implant surface to those emitted from the bulk plasma, we additionally obtained the emission spectrum at zone 2, as shown in Figure S3. Compared with the emissions in zone 1, the peak intensities of the N_2 and N_2^+ emission spectra in zone 2 were approximately 20 times and 500 times lower, respectively. This suggests that the density of vibrationally excited N_2 molecules and N_2^+ ions within the implant surface region was significantly greater than that in the bulk region, indicating a greater energetic

and reactive species density within the implant surface region[43,44]. Given that the implant serves as part of the ground electrode, the plasma at the implant surface is likely part of the plasma sheath. Therefore, the observed high plasma density at the implant surface compared with that in the bulk region seems to be reasonable.

Rotational and vibrational temperatures

On the basis of the intensity distributions of the measured spectra, we estimated the rotational temperature of N_2^+ and the vibrational temperature of excited N_2 to investigate the relation between the plasma and the pressure condition. The spectrum of the N_2^+ first negative system was used to determine the rotational temperature, which is generally considered equivalent to the gas temperature[45]. LIFBASE Spectroscopy Tool was used to simulate the spectrum and compare it with the measured spectra to estimate the rotational temperature[46]. To determine the vibrational temperature of N_2, we employed the line ratio method using the peak intensities at 380.5 nm and 375.6 nm. This method is applicable for plasmas discharged in the pressure range used in this work, where electron impact is the predominant pathway for vibrational excitation[47–49]. The relation for intensity ratio is derived from Eq. 6 in reference 47 (Fatima et al., 2021), utilizing the 375.54 nm line intensity and spectral constant instead of 371.05 nm[47].

$$\frac{I_{1v'\,v''}\ (375.5\ \mathrm{nm})}{I_{2v'\,v''}\ (380.5\ \mathrm{nm})} = 1.399e^{-\frac{0.292}{T_{\mathrm{vib}}}} \tag{1}$$

The rotational temperature of zone 1 was measured at 520 ± 10 K under both 10s- and 20s-pumping conditions and did not significantly change over time (a representative spectral fitting is shown in Figure S4 [45]). The time-averaged vibrational temperatures were approximately 5050 ± 227 K and 5264 ± 243 K under 16 Torr and 5 Torr conditions, respectively (see Figure S5). Although the average vibrational temperature under the 20s-pumping condition was slightly higher than that under the 10s-pumping condition, the difference remained within the error range. Under both the 16 Torr and 5 Torr conditions, the fluctuation in the vibrational temperature was not significant, and the temporal changes did not appear to have a particular pattern. These observations indicate that the pre-pumping time or the pressure at the time of discharge did not significantly influence the vibrational temperature.

In zone 2, estimating the rotational temperature was challenging due to the low intensity of N_2^+ emission. The time-averaged vibrational temperature was measured to be approximately 4491 ± 372 K and 4440 ± 190 K under 16 Torr and 5 Torr conditions, respectively (Figure S5). Notably, the fluctuation in vibrational temperature under the 5 Torr condition was lower than that under the 16 Torr condition, suggesting that the vibrational temperature of the bulk plasma becomes more stable with longer pre-pumping durations.

The vibrational temperature in zone 1 was higher than that in zone 2. This shows that the electron temperature and the density of vibrationally excited N_2 molecules in zone 1 are certainly greater those that in zone 2 [52,53]. This result reveals localized differences in plasma characteristics and supports our previous findings that the implant surface region (zone 1) has higher plasma density than does the bulk region (zone 2).

Peak intensity profile

The temporal changes in peak intensity were monitored under the 16 Torr and 5 Torr conditions, as shown in Fig. 4. In the plasma at the implant surface (zone 1), the emission intensity drastically declined under the 16 Torr condition. This decline in emission intensity appears to align with the trend in the pressure profile of the vacuum chamber provided in Fig. 2. As the pressure decreases over time, there is a reduction in the number of neutral gas molecules available for excitation within the plasma, leading to a corresponding decline in emission intensity. Therefore, the observed decrease in emission intensity is expected to parallel the reducing gas pressure. Conversely, under the 5 Torr condition, the emission intensity decreased slightly by approximately 14% but maintained relatively stable, as the gas pressure remained relatively constant. As a result, the emission light intensity immediately after plasma breakdown was greater in the 16 Torr case, but the overall emission intensity after 3 s of breakdown was greater in the plasma under the 5 Torr condition, presumably due to the greater stability of the plasma under these conditions.

The plasma in zone 2 does not directly contact the implant surface; however, to investigate the overall stability of the discharge, the plasma intensity in zone 2 was also monitored. In zone 2, the peak intensity increased over time under both the 16 Torr and 5 Torr conditions, as shown in Fig. 4C and D. This result is likely due to the improved plasma stability over time. As shown in Fig. 1C, under the 16 Torr condition, the width of the plasma column was initially smaller (at approximately 1 and 2 s) but expanded over time. Additionally, the plasma was much denser in the top and bottom regions of the column (indicated with white circles in Fig. 1C) at the initial time but gradually spread out and became more uniform. In contrast, under the 5 Torr condition, the plasma appeared to be stably discharged from the beginning, as evidenced by the uniform plasma volume and consistent emission across the entire plasma column.

Another notable difference in the discharge images was the presence of striations in the plasma column. Specifically, the 5 Torr case exhibited clearer striations. Previous studies have shown that striations can form in the positive column region of glow discharge[52,53]. These striations are caused by fluctuations in electron and ion densities, which are pressure-dependent[52]. According to Lisovsky et al., the thickness of the striations is inversely proportional to pressure, which explains why the 5 Torr case (with lower pressure) exhibited thinner and more striations. In contrast, under the 16 Torr condition, as the pressure steadily decreased from 16 torr to 5 torr during plasma discharge, the striation pattern likely fluctuated, reducing the stability and clarity of the striations.

Despite the stability observed under the 5 Torr condition, the intensity of the N_2 emission (315.8 nm and 337.2 nm) continued to increase (Fig. 4D). We speculate that this increase is due to the gradual accumulation of excited molecules over time as a result of the temperature increase caused by continuous discharge[54]. Overall,

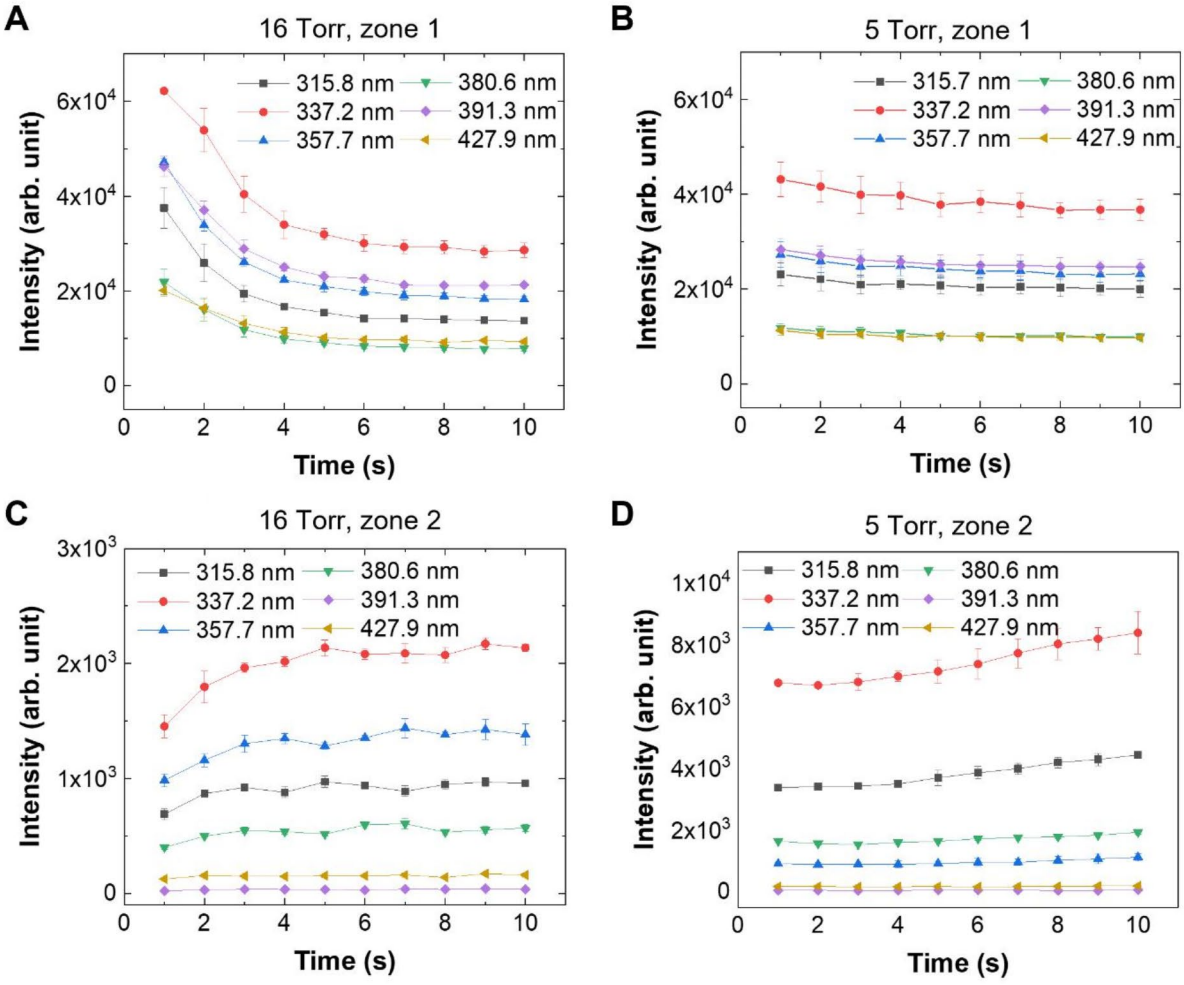

Fig. 4. The temporal change in peak intensity of all measured wavelengths: Zone 1 in (**A**) 16 Torr, and (**B**) 5 Torr condition; Zone 2 in (**C**) 16 Torr, and (**D**) 5 Torr condition.

these results suggest that the 5 Torr condition can more effectively treat the implant surface during the 10s-plasma treatment period by creating an environment conductive to a more stable plasma discharge.

To gain further insight into electron density, we referred to one of our previous studies, where we numerically analyzed the relationship between pressure, electron temperature, and electron density in plasma[1]. Our findings demonstrated a clear correlation between pressure and the generation of high-energy electrons. Plasma generated at 5 Torr produced a higher number of high-energy electrons (> 15 eV) compared to plasma at 15 Torr[1]. According Thiébaut, J. M. et al., the lowest threshold energy required to dissociate the simplest hydrocarbon impurities (CH_4) is 12.63 eV[55]. Therefore, the high-energy electrons generated at low pressure (5 Torr) are particularly effective at breaking hydrocarbon bonds and removing surface impurities. Based on these findings, we can reasonably infer that the plasma discharged at 5 Torr in the current study likely facilitated more efficient dissociation of hydrocarbon impurities compared to plasma discharged under 16 Torr condition. This inference also aligns with the higher N_2 emissions observed under the 5 Torr condition compared to 16 Torr condition.

Building on our plasma emission spectroscopy observations and the above discussions, we extended our investigation to understand how the tested plasma conditions (16 Torr and 5 Torr) influence surface modification and the resulting biological effects. Previous studies have demonstrated that surface hydrophilicity is significantly enhanced when surface hydrocarbon-based impurities are removed from the titanium surface, which in turn facilitates osteoblast activity and osseointegration[20,21]. Similarly, to investigate the links among plasma discharge conditions, plasma-induced surface modifications, and the resulting effects on osteoblast activity, we first assessed surface hydrophilicity and surface chemical composition.

Wettability of the implant surface

Surface hydrophilicity is one of the key characteristics that may degrade due to surface aging during the shelf storage of medical implants[56]. To evaluate surface hydrophilicity, we examined the wetting process of the implant surface using distilled water (DW). Due to the threaded structure of the implants, quantifying wettability through contact angle measurements was not feasible. Instead, we immersed the bottom part of the implant in a DW

reservoir and allowed the DW to wet the implant surface (see Fig. 5). This method allowed us to qualitatively assess the wettability of the implant surfaces[57,58]. By recording the process of DW wetting and ascension along the threads of the implants on video and analyzing the wetting speed, we evaluated the hydrophilicity of the implant surface.

Figure 5 presents a snapshot obtained from the recorded video of the control implant, where the DW did not wet the implant surface at all (Fig. 5A). In contrast, in the case of the plasma-treated implants, the DW ascended

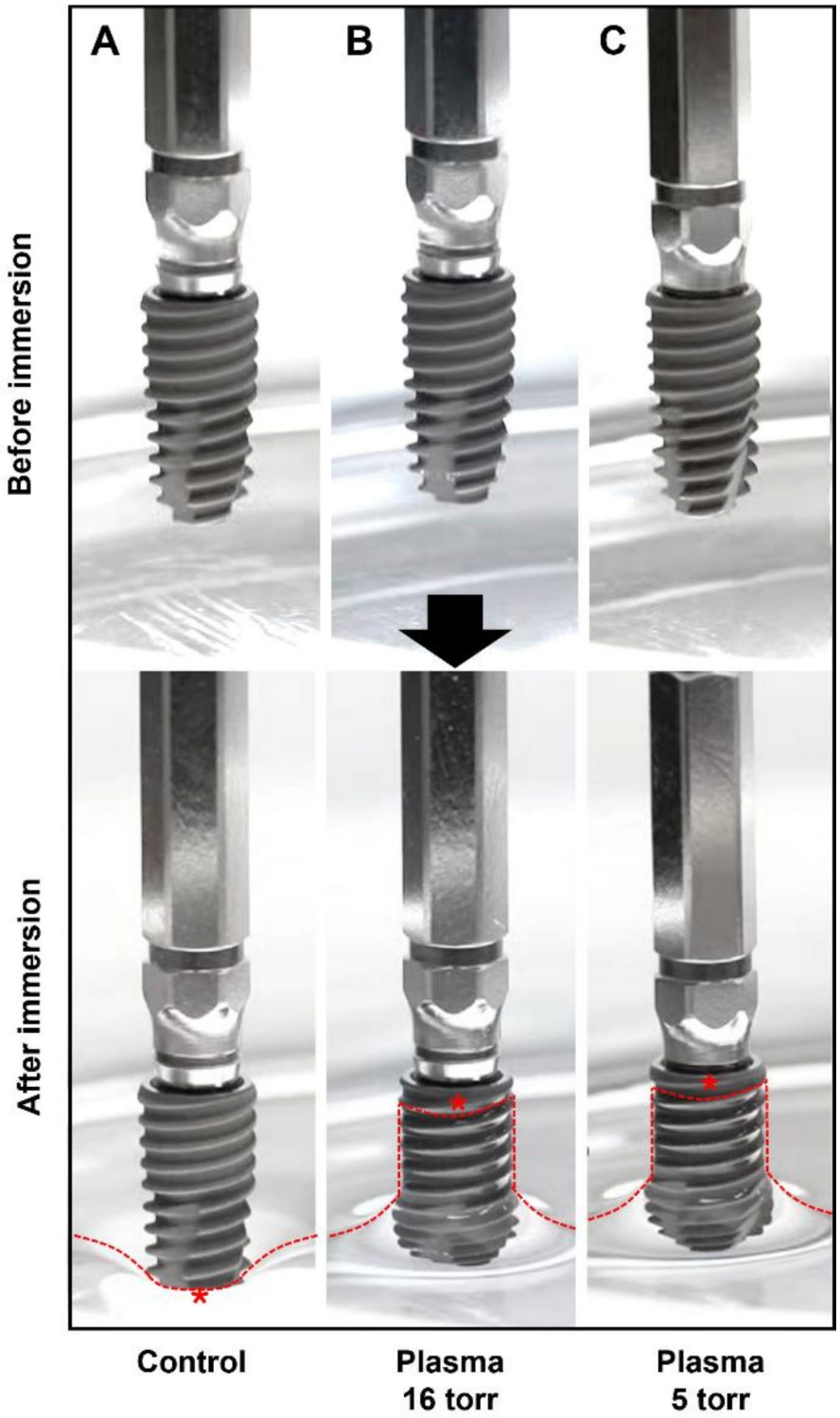

Fig. 5. Wettability of implants for (**A**) control, (**B**) plasma-treated under 16 Torr, and (**C**) plasma-treated under 5 Torr conditions. For both the 16 Torr and 5 Torr conditions, the plasma treatment time was 10 s.

along the implant thread, with no discernible difference between the 16 Torr and 5 Torr conditions (Fig. 5B and C). The red dotted lines indicate the water level, and the asterisks (*) show the highest point of DW ascension. To confirm the persistence of hydrophilicity, the same experiment was conducted one hour after plasma treatment. As shown in Figure S6, the hydrophilicity was maintained even after one hour. While these findings align with those of previous studies suggesting that plasma treatment enhances the hydrophilicity of the implant surface, there was no observable difference due to the two different plasma conditions. However, it remains uncertain whether this lack of a difference is genuine or a result of the limitations in our measurement method, as subtle variations in wettability may not be distinguishable.

Previous reports have shown that TiO_2 surfaces can be made hydrophilic through electrostatic modification[42,59]. These reports explain that surface treatment can generate oxygen vacancies on the TiO_2 surface, converting Ti^{4+} sites to Ti^{3+} sites, which are favorable for water adsorption. Similarly, plasma treatments, particularly those that create nitrogen radicals, are known to induce oxygen vacancies in TiO_2, thereby increasing its hydrophilicity[60,61].

Chemical composition of the implant surface

To evaluate the efficiency of impurity removal from the implant surface by plasma treatment, changes in atomic concentration were assessed using XPS. XPS analysis revealed peaks corresponding to Ti2p, C1s, and O1s (Table S1). As shown in Fig. 6, the proportions of carbon on the implant surface for the control, 16 Torr plasma-treated, and 5 Torr plasma-treated conditions were $21.54 \pm 1.21\%$, $21.07 \pm 1.25\%$, and $17.29 \pm 0.64\%$, respectively. The proportion of carbon was significantly reduced by 19.73% in the implants treated with plasma under the 5 Torr condition compared with the control, while it did not differ much in the implants treated with plasma under the 16 Torr condition. This finding indicates that plasma treatment under the 5 Torr condition effectively removed carbon-based impurities from the implant surface, whereas plasma treatment under the 16 Torr condition was not sufficiently effective. The measured proportion of oxygen for the control, 16 Torr plasma-treated, and 20s-pumping plasma-treated conditions were $58.81 \pm 0.42\%$, $58.20 \pm 0.42\%$, and $61.20 \pm 0.24\%$, respectively. The proportion of oxygen in the implants treated under the 5 Torr condition increased by 3.89% compared to the control. Although this change was not large, it was statistically significant, whereas the implants treated under the 16 Torr condition did not exhibit any significant change compared with the control.

Several reactions may be involved in the removal of carbon-based impurities, as indicated by previous studies. Upon exposure to plasma, hydrocarbon pellicles deposited on the implant surface react with excited nitrogen species, oxygen species, and other reactive species within the plasma[27,62]. Since the background gas was air in our experiments, it is likely that a significant portion of the carbon-based impurities were removed by excited nitrogen species. The reaction can be written as[27]:

$$C_xH_yO_z + \ (N,\ N_2{}^*) \rightarrow CN + NH + NO \tag{2}$$

where $C_xH_yO_z$ represents a general hydrocarbon molecule and (N, N_2^*) denotes reactive nitrogen species and excited nitrogen species. The excited nitrogen species not only generate reaction products but also break C-H bonds and induce conformational changes in impurities[27]. Therefore, reaction (2) implies that the density of vibrationally-excited molecules is an important parameter for impurity removal.

Our findings show that the 5 Torr condition significantly reduced the carbon content on the implant surface by 19.73%, while the 16 Torr condition had a weaker effect. This discrepancy can be explained by differences in the plasma emission intensity between the 5 Torr and 16 Torr conditions. The plasma under 5 Torr pumping appears to maintain higher and more stable densities of excited nitrogen species, as demonstrated by the consistent and higher time-averaged emission intensity observed in the plasma emission spectrum analysis.

Moreover, as shown in Fig. 1C and D, the plasma covered the entire implant surface under the 5 Torr condition throughout the 10-second plasma treatment. In contrast, under the 16 Torr condition, the plasma coverage was initially localized at the top area of the implant and gradually expanded over time. The stable plasma environment achieved under the 5 Torr condition ensures that the vibrationally excited nitrogen species uniformly interact with and effectively remove carbon impurities from the implant surface.

Cellular activities

On the basis of the above findings, we further investigated the biological performance of all the samples, including the control, plasma-16 Torr, and plasma-5 Torr groups. Interactions between the implant and biological tissue, particularly at the bone–implant interface, are crucial for osteoblastic activity and osseointegration[63–65]. Proteins play a crucial role in forming this interface; once adsorbed, they form a layer on the implant surface that can regulate cellular adhesion and activities[66,67]. Previous studies have identified fibronectin and vitronectin as key proteins in this process[20,68,69]. In our study, we focused on fibronectin. As illustrated in Fig. 7A, implants treated with plasma under the 16 Torr condition presented an 11.9% increase in the amount of fibronectin adsorbed compared with the nontreated control implants; however, this increase was not statistically significant. In contrast, implants treated with plasma under the 5 Torr condition presented a 17.8% increase in the amount of fibronectin adsorbed relative to the control group, which was statistically significant. These results suggest that plasma treatment with 5 Torr condition can significantly enhance ECM protein adsorption on the implant surface, thereby resulting in a more favorable environment for cellular adhesion.

As discussed previously, implant surfaces composed of TiO_2 can acquire hydrophilic properties through exposure to nitrogen radicals within plasma. Materials with a more hydrophilic surface have been found to have an enhanced affinity for proteins[42]. In addition, studies have demonstrated that the removal of hydrocarbons further improves protein affinity[60,70]. These findings are consistent with our results from the wettability test and XPS analysis, which revealed a substantial increase in wettability and a significant decrease in carbon content under the 5 Torr condition. Hence, the observed increase in protein adsorption observed under the 5 Torr

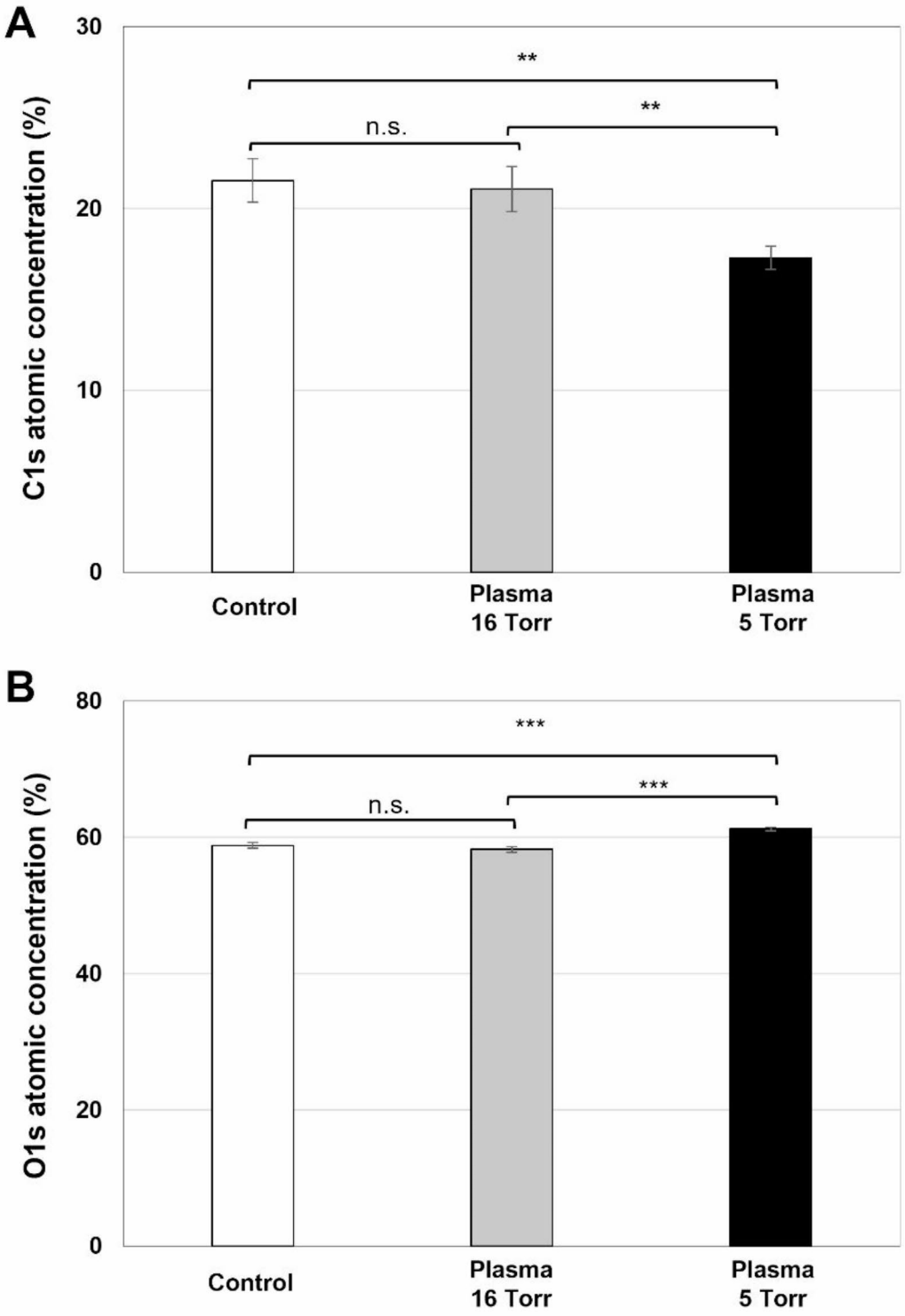

Fig. 6. Atomic concentration of (**A**) C1 and (**B**) O1s on implant surfaces for control, plasma-treated under 16 Torr, and plasma-treated under 5 Torr conditions. For both the 16 Torr and 5 Torr conditions, the plasma treatment time was 10 s. [$^{**}P < 0.01$, $^{***}P < 0.001$, n.s.(not significant) > 0.05].

condition appears to be associated with enhanced hydrophilicity and reduced hydrocarbon impurities on the implant surface.

Given that enhanced protein adsorption has been shown to improve osseointegration and overall implant performance, we then examined the efficiency of cellular attachment and proliferation on the control and plasma-treated implants (under 16 Torr and 5 Torr conditions). For all plasma-treated in vitro groups, the plasma

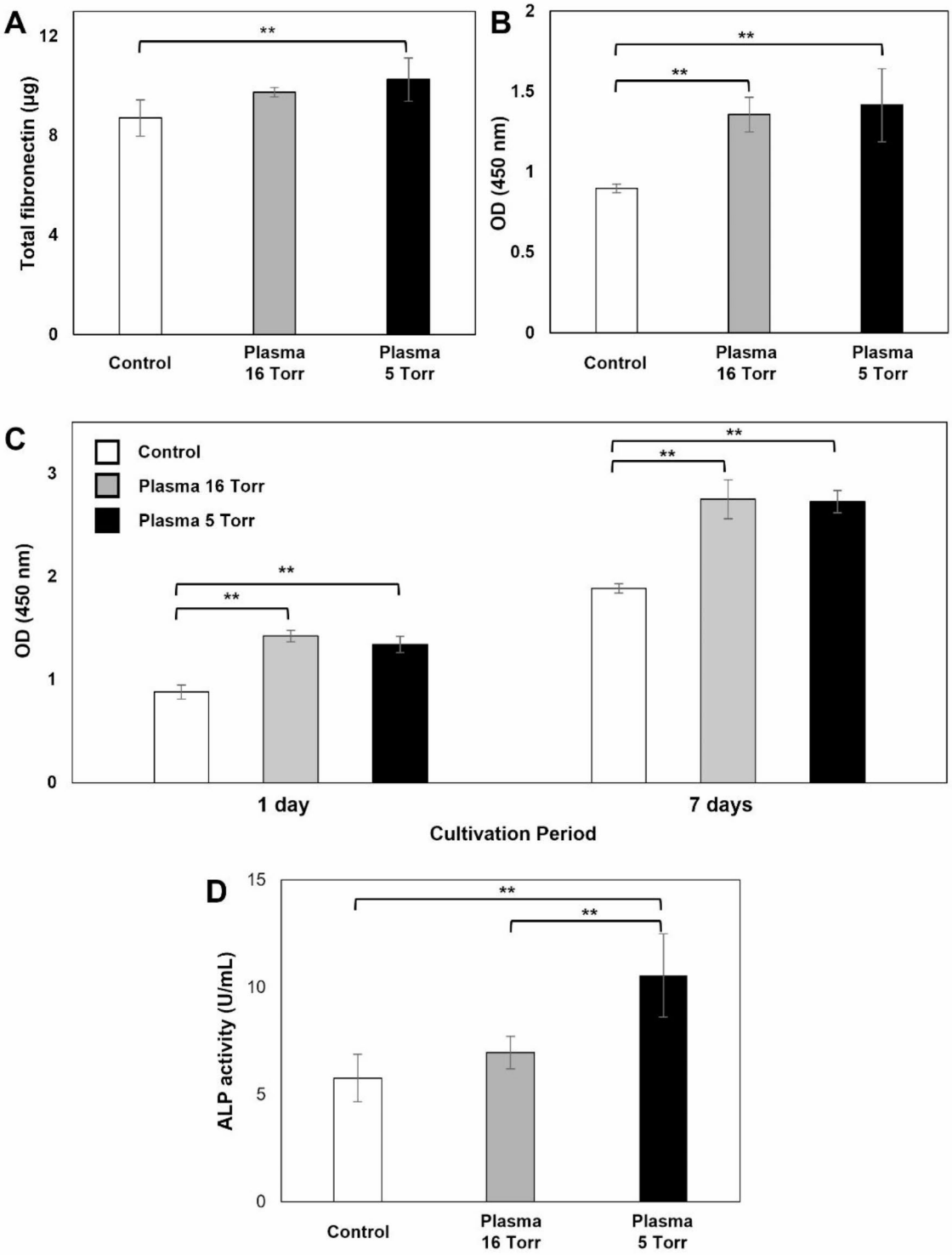

Fig. 7. In vitro experiments comparing control, plasma-treated under 16 Torr, and plasma-treated under 5 Torr conditions. For both the 16 Torr and 5 Torr conditions, the plasma treatment time was 10 s. (**A**) The amount of adsorbed fibronectin on implant surfaces, (**B**) the number of cells attached to the implant surfaces within 2 h, (**C**) cell proliferation at day 1 and day 7, and (b) ALP activity at day 7. [$^{*}P < 0.05$, $^{**}P < 0.01$, $^{***}P < 0.001$, n.s.(not significant) > 0.05].

treatment was applied for 10 s following pumping times of either 10–20 s. As previously noted, the 10-second pumping corresponds to the 16 Torr condition, and the 20-second pumping corresponds to the 5 Torr condition. To evaluate early cellular attachment, we quantified the number of cells attached to the implant surfaces within two hours using the CCK-8 assay, as shown in Fig. 7B. The number of adherent cells increased by 51.1% and 57.5% on the plasma-treated implants under the 16 Torr and 5 Torr conditions, respectively, compared to the control implants.

To assess the degree of cellular proliferation on each implant surface, we measured the number of cells on days 1 and 7 post-attachment, as shown in Fig. 7C. On day 1, cell proliferation on the plasma-treated implants increased by 61.6% and 52.5% under the 16 Torr and 5 Torr conditions, respectively, compared with that of the control. By day 7, cell proliferation exhibited a 45.8% increase for the 16 Torr condition and a 44.6% increase for the 5 Torr condition, relative to the control group. According to the results of the cell attachment experiments, both plasma treatments (16 Torr and 5 Torr conditions) significantly improved initial cell adhesion to the implant. When comparing the two plasma treatment conditions, the 5 Torr condition was more effective than the 16 Torr condition. In terms of cellular proliferation over a prolonged incubation period, both plasma treatments improved proliferation efficiency compared with that of the control, but there was no noticeable difference between the two plasma-treated groups.

To investigate the differentiation efficiency, which is essential for osseointegration, the ALP activity in cells grown on the implants was measured (Fig. 7D). The ALP activity of cells on the plasma-treated implants increased by 20.6% and 82.7% under the 16 Torr and 5 Torr conditions, respectively, compared to the value for the control implant. This indicates that plasma treatment enhances osteoblast differentiation and further demonstrates that plasma treatment under the 5 Torr condition was more efficient than treatment under the 16 Torr condition at promoting osteoblast differentiation.

When comparing these findings with the proliferation results, we observed a slight difference in trends. However, in previous studies, it is well known that cell proliferation and differentiation can follow distinct trends as they represent different cellular processes. Even when proliferation rates are comparable, osteoblasts can exhibit enhanced differentiation under specific environmental conditions[71,72] Given that cellular differentiation plays a crucial role in in vivo applications, as supported by numerous animal studies where osteogenic differentiation is key to tissue integration and healing[20,40], we anticipate that the 5 Torr condition will likely provide superior osseointegration performance both in vivo and in clinical settings.

Finally, we observed the cellular morphology and distribution on the implants via fluorescence labeling of cells. The cell image data corroborated the cellular responses observed above. After cells were attached to the implant surface, they were cultured for 7 days, fixed, and fluorescently labeled. Cell nuclei (gray) were labeled with Hoechst, and actin (red) was labeled with phalloidin (Fig. 8, Figure S7). During the cell attachment process, the implants were submerged vertically into the cell suspension. Due to gravitational force, cells initially settled on top of the implant threads and then spread to neighboring surfaces as they proliferated. In the control implants (Fig. 8A), the majority of cells attached at the edges of the threads, leaving many areas devoid of cells. As indicated by the white arrowhead in Fig. 8A, some cells attached to the control implant did not fully spread on the implant surface, exhibiting a rounded shape rather than an elongated shape with distinct actin stress fibers. This rounded shape is further highlighted in the enlarged images shown in the supplementary figure (Figure S7). Figure 8B and C show cells attached to plasma-treated implants. These implants exhibit more uniform cell coverage; however, as expected from the cell proliferation data, the cell density did not noticeably differ between the 16 Torr and 15 Torr conditions. The enlarged images in Figure S7 show, as indicated by the white arrowheads, that the actin stress fibers in cells attached to the plasma-treated surfaces are more prominent compared to those on the control implant surface.

Based on the overall in vitro experimental results, plasma treatment demonstrated significant benefit for protein adsorption, which facilitated subsequent cell adhesion[73,74]. This was evidenced by the uniform cell coverage and well-spread cell morphology observed in the fluorescence images. These improvements in cell adhesion can ultimately contribute to increased proliferation[75,76]. Given the role of osteoblasts in bone formation, these findings suggest that plasma treatment significantly supports the osseointegration process, aligning with previous studies on implant surface modification[1,20,42]. Furthermore, the ALP assay results revealed a notable increase in osteoblast differentiation under the 5 Torr condition compared to the 16 Torr condition. This suggests that plasma treatment at 5 Torr, which stably generates excited nitrogen radicals, not only improves hydrocarbon removal but also enhances bone differentiation, thereby increasing the potential for successful osseointegration.

In this study, we aimed to identify the key factors driving plasma-mediated implant surface modification and determine optimal operating conditions for maximizing plasma performance. To achieve this, we compared two representative operational conditions: 16 Torr achieved by 10 s pre-pumping and 5 Torr achieved by 20 s pre-pumping. Plasma characteristics are influenced by several factors, such as electrode gap distance, driving power, and chamber/electrode geometry, meaning that optimal pressure conditions may vary based on these specific configurations. Despite these influencing factors, under our current experimental setup, we identified excited nitrogen radicals as the primary factor contributing to plasma surface treatment performance. Furthermore, our findings demonstrated that the 5 Torr condition provided the optimal environment for controlling these radicals. This 5 Torr condition maximizes the surface treatment effects, as it significantly outperformed the 16 Torr condition in terms of carbon-based impurity removal and osteoblast differentiation.

In summary, the observed improvements in osteoblast activity can be attributed to the synergistic effects of increased surface hydrophilicity, effective hydrocarbon removal, and enhanced protein adsorption. The excited nitrogen radicals generated within the plasma created a surface that is highly favorable for osteoblast adhesion and differentiation. Consequently, our study highlights the critical role of stable plasma discharge and the control of excited nitrogen radicals in promoting osteoblast activity and differentiation. By optimizing

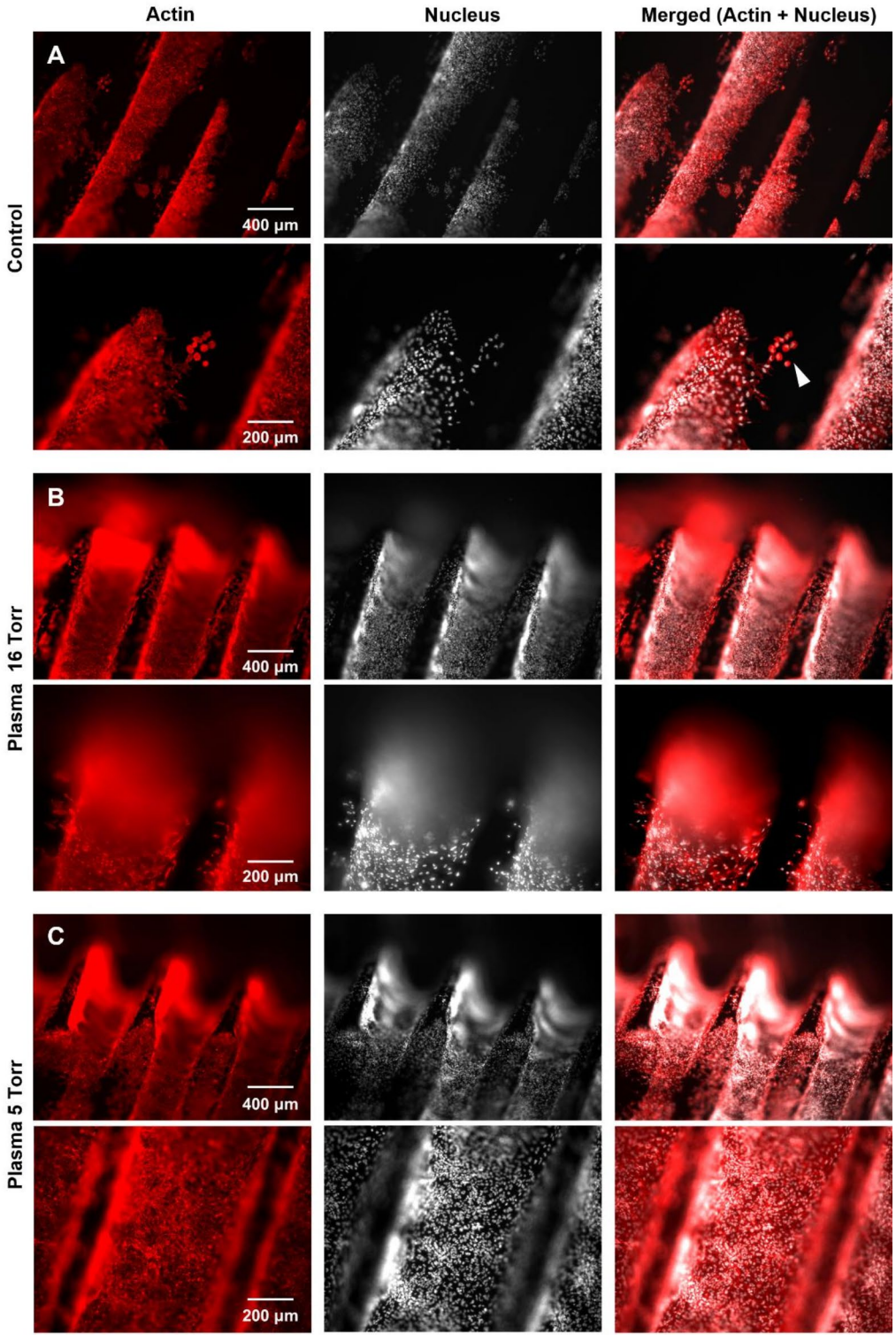

Fig. 8. Fluorescence images of cells on implant surfaces for (**A**) control, (**B**) plasma-treated under 16 Torr, and (**C**) plasma-treated under 5 Torr conditions. For both the 16 Torr and 5 Torr conditions, the plasma treatment time was 10 s. Actin stress fibers are shown in red (Rhodamine phalloidin) in the first column, nuclei are shown in gray (Hoechst 33342) in the second column, and the merged image of the nucleus and actin in the third column.

operational conditions to effectively control these radicals, vacuum-assisted plasma treatment technology has the potential to offer substantial clinical benefits, not only for dental implants but also for other metal implants.

Conclusions

In conclusion, our study demonstrates that the 5 Torr plasma treatment condition significantly enhances the biological performance of implant surfaces. The stable generation of excited nitrogen species during this treatment leads to beneficial modifications in surface chemistry, which in turn improve hydrophilicity, reduce hydrocarbon impurities, and increase protein adsorption. These changes collectively create an optimal environment for cellular attachment, proliferation, and differentiation, thereby promoting osseointegration. This study provides valuable insights into the mechanisms by which plasma treatment enhances implant performance and highlights the potential for further optimization of plasma treatment parameters to maximize clinical outcomes in dental and orthopedic applications.

Data availability

The original data in this article will be shared upon reasonable request to the corresponding authors.

Received: 15 August 2024; Accepted: 9 December 2024
Published online: 30 December 2024

References

1. Lee, H. et al. Improvement of osseointegration efficacy of titanium implant through plasma surface treatment. *Biomed. Eng. Lett.* **12**, 421–432. https://doi.org/10.1007/s13534-022-00245-9 (2022).
2. Lee, J. H. et al. Non-thermal atmospheric pressure plasma functionalized dental implant for enhancement of bacterial resistance and osseointegration. *Dent. Mater.* **33**, 257–270. https://doi.org/10.1016/j.dental.2016.11.011 (2017).
3. Das, S. et al. Efficacy of argon cold atmospheric pressure plasma jet on hospital surface decontamination and its impact on the surface property. *Phys. Scr.* **99** https://doi.org/10.1088/1402-4896/ad1869 (2024).
4. Laroussi, M. Sterilization of contaminated matter with an atmospheric pressure plasma. *Ieee T Plasma Sci.* **24**, 1188–1191 (1996).
5. Abramzon, N., Joaquin, J. C., Bray, J. & Brelles-Marino, G. Biofilm destruction by RF high-pressure cold plasma jet. *Ieee T Plasma Sci.* **34**, 1304–1309 (2006).
6. Das, S. et al. Antimicrobial efficacy of argon cold atmospheric pressure plasma jet on clinical isolates of multidrug-resistant ESKAPE Bacteria. *IEEE Trans. Radiat. Plasma Med. Sci.* **7**, 421–428. https://doi.org/10.1109/trpms.2023.3235358 (2023).
7. Das, S., Mohapatra, S. & Kar, S. Elucidating the bacterial inactivation mechanism by argon cold atmospheric pressure plasma jet through spectroscopic and imaging techniques. *J. Appl. Microbiol.* **135**, 13. https://doi.org/10.1093/jambio/lxae238 (2024).
8. Nastuta, A. V., Topala, I., Grigoras, C., Pohoata, V. & Popa, G. Stimulation of wound healing by helium atmospheric pressure plasma treatment. *J. Phys. D Appl. Phys.* **44**, 105204 (2011).
9. Lee, D. H. et al. Suppression of scar formation in a murine burn wound model by the application of non-thermal plasma. *Appl. Phys. Lett.* **99**, 203701 (2011).
10. Kong, M. G. et al. Plasma medicine: An introductory review. *New. J. Phys.* **11**, 115012 (2009).
11. Lloyd, G. et al. Gas plasma: medical uses and developments in wound care. *Plasma Process. Polym.* **7**, 194–211 (2010).
12. Gweon, B. et al. Differential responses of human liver cancer and normal cells to atmospheric pressure plasma. *Appl. Phys. Lett.* **99**, 063701 (2011).
13. Kim, K. et al. Suppression of breast cancer cell migration and epithelial-mesenchymal transition by atmospheric pressure plasma. *Front. Phys.* **9**, 8. https://doi.org/10.3389/fphy.2021.694080 (2021).
14. Chu, P. K., Chen, J. Y., Wang, L. P. & Huang, N. Plasma-surface modification of biomaterials. *Mater. Sci. Eng. R-Rep.* **36**, 143–206. https://doi.org/10.1016/s0927-796x(02)00004-9 (2002).
15. Yang, J. X., Cui, F. Z., Lee, I. S. & Wang, X. M. Plasma surface modification of magnesium alloy for biomedical application. *Surf. Coat. Technol.* **205**, S182–S187. https://doi.org/10.1016/j.surfcoat.2010.07.045 (2010).
16. Silva, S. S. et al. Plasma surface modification of chitosan membranes: Characterization and preliminary cell response studies. *Macromol. Biosci.* **8**, 568–576. https://doi.org/10.1002/mabi.200700264 (2008).
17. Barfeie, A., Wilson, J. & Rees, J. Implant surface characteristics and their effect on osseointegration. *Br. Dent. J.* **218**, E9. https://doi.org/10.1038/sj.bdj.2015.171 (2015).
18. Zhu, G., Wang, G. & Li, J. J. Advances in implant surface modifications to improve osseointegration. *Mater. Adv.* **2**, 6901–6927. https://doi.org/10.1039/d1ma00675d (2021).
19. Nobles, K. P., Janorkar, A. V. & Williamson, R. S. Surface modifications to enhance osseointegration-resulting material properties and biological responses. *J. Biomed. Mater. Res. B Appl. Biomater.* **109**, 1909–1923. https://doi.org/10.1002/jbm.b.34835 (2021).
20. Aita, H. et al. The effect of ultraviolet functionalization of titanium on integration with bone. *Biomaterials* **30**, 1015–1025. https://doi.org/10.1016/j.biomaterials.2008.11.004 (2009).
21. Jeon, H. J. et al. Enhanced osteoblast adhesion and proliferation on Vacuum plasma-treated Implant Surface. *Appl. Sci-Basel.* **12**, 13. https://doi.org/10.3390/app12199884 (2022).
22. Nevins, M., Chen, C. Y., Parma-Benfenati, S. & Kim, D. M. Gas plasma treatment improves titanium dental implant osseointegration-a preclinical in vivo experimental study. *Bioeng. (Basel).* 10. https://doi.org/10.3390/bioengineering10101181 (2023).
23. Soltanzadeh, P. et al. Success rate and strength of osseointegration of immediately loaded UV-photofunctionalized implants in a rat model. *J. Prosthet. Dent.* **118**, 357–362. https://doi.org/10.1016/j.prosdent.2016.11.008 (2017).
24. Hui, W. L., Perrotti, V., Iaculli, F., Piattelli, A. & Quaranta, A. The emerging role of cold atmospheric plasma in implantology: A review of the literature. *Nanomaterials-Basel* 10 (2020).
25. Tsujita, H., Nishizaki, H., Miyake, A., Takao, S. & Komasa, S. Effect of plasma treatment on titanium surface on the tissue surrounding implant material. *Int. J. Mol. Sci.* **22**, ARTN. https://doi.org/10.3390/ijms22136931 (2021).
26. Hori, M. Radical-controlled plasma processes. *Rev. Mod. Plasma Phys.* **6**, 117. https://doi.org/10.1007/s41614-022-00084-2 (2022).
27. Thiébaut, J. M. et al. Comparison of surface cleaning by two atmospheric pressure discharges. *Surf. Coat. Technol.* **169**, 186–189. https://doi.org/10.1016/s0257-8972(03)00043-4 (2003).
28. Zaplotnik, R., Kreuh, D., Vesel, A., Removal of surface & impurities from qcm substrates with the low-pressure oxygen-plasma treatment. *Mater. Tehnol* **47**, 795–797 (2013).
29. Roy, M. et al. Photofunctionalization of Titanium: an alternative explanation of its chemical-physical mechanism. *PloS One.* **11**, 11. https://doi.org/10.1371/journal.pone.0157481 (2016).

30. Hanson, D. M., Stockbauer, R., Madey, T. E., The interaction of & methanol with a titanium(001) surface investigated using photon stimulated desorption and UV photoemission spectroscopy. *J. Chem. Phys.* **77**, 1569–1575, doi:https://doi.org/10.1063/1.443939 (1982).
31. Henningsen, A. et al. Photofunctionalization and non-thermal plasma activation of titanium surfaces. *Clin. Oral Investig.* **22**, 1045–1054. https://doi.org/10.1007/s00784-017-2186-z (2018).
32. Smeets, R. et al. Influence of ultraviolet irradiation and cold atmospheric pressure plasma on zirconia surfaces: An in vitro study. *Int. J. Oral Max Impl.* **34**, 329–336. https://doi.org/10.11607/jomi.7017 (2019).
33. Matsumoto, T. et al. Effects of surface modification on adsorption behavior of cell and protein on titanium surface by using quartz crystal microbalance system. *Mater. (Basel).* **14** https://doi.org/10.3390/ma14010097 (2020).
34. Kim, M. C., Yang, S. H., Boo, J. H. & Han, J. G. Surface treatment of metals using an atmospheric pressure plasma jet and their surface characteristics. *Surf. Coat. Technol.* **174–175**, 839–844. https://doi.org/10.1016/s0257-8972(03)00560-7 (2003).
35. Noh, J. H., Baik, H. K., Noh, I., Park, J. C. & Lee, I. S. Surface modification of polytetrafluoroethylene using atmospheric pressure plasma jet for medical application. *Surf. Coat. Technol.* **201**, 5097–5101. https://doi.org/10.1016/j.surfcoat.2006.07.223 (2007).
36. Gonzalez, E. 2nd & Hicks, R. F. Surface analysis of polymers treated by remote atmospheric pressure plasma. *Langmuir* **26**, 3710–3719. https://doi.org/10.1021/la9032018 (2010).
37. Bónová, L. et al. Atmospheric pressure plasma treatment of flat aluminum surface. *Appl. Surf. Sci.* **331**, 79–86. https://doi.org/10.1016/j.apsusc.2015.01.030 (2015).
38. Coelho, P. G. et al. Argon-based atmospheric pressure plasma enhances early bone response to rough titanium surfaces. *J. Biomed. Mater. Res. A.* **100**, 1901–1906. https://doi.org/10.1002/jbm.a.34127 (2012).
39. Canullo, L. et al. Hard and soft tissue changes around implants activated using plasma of argon: A histomorphometric study in dog. *Clin. Oral Implants Res.* **29**, 389–395. https://doi.org/10.1111/clr.13134 (2018).
40. Ryu, D. J. et al. Enhanced osseointegration through direct energy deposition porous coating for cementless orthopedic implant fixation. *Sci. Rep-Uk*. **11**, 12. https://doi.org/10.1038/s41598-021-01739-9 (2021).
41. Hempel, U., Hefti, T., Dieter, P. & Schlottig, F. Response of human bone marrow stromal cells, MG-63, and SaOS-2 to titanium-based dental implant surfaces with different topography and surface energy. *Clin. Oral Implants Res.* **24**, 174–182. https://doi.org/10.1111/j.1600-0501.2011.02328.x (2013).
42. Iwasa, F. et al. Enhancement of osteoblast adhesion to UV-photofunctionalized titanium via an electrostatic mechanism. *Biomaterials* **31**, 2717–2727. https://doi.org/10.1016/j.biomaterials.2009.12.024 (2010).
43. Qayyum, A. et al. Optical emission spectroscopy of the active species in nitrogen plasma. *Plasma Devices Oper.* **14**, 61–70. https://doi.org/10.1080/10519990500281659 (2006).
44. Hino, T., Yamauchi, Y., Ono, J. & Hirohata, Y. Enhancement of reactive species density in nitrogen plasma by mixture of helium and nitridation experiment for silicon. *Vacuum* **74**, 467–471. https://doi.org/10.1016/j.vacuum.2004.01.016 (2004).
45. Moon, S. Y. & Choe, W. A comparative study of rotational temperatures using diatomic OH, OH, O_2 and N_2^+ molecular spectra emitted from atmospheric plasmas. *Spectroc Acta Pt B-Atom Spectr.* **58**, 249–257. https://doi.org/10.1016/s0584-8547(02)00259-8 (2003).
46. Luque, J. & Crosley, D. R. LIFBASE: Database and spectral simulation program (version 1.5) (SRI Int., Menlo Park, CA, USA, Tech. Rep. MP99-009, 1999).
47. Fatima, H. et al. Spectroscopic evaluation of vibrational temperature and electron density in reduced pressure radio frequency nitrogen plasma. *Sn Appl. Sci.* **3**, 11. https://doi.org/10.1007/s42452-021-04651-z (2021).
48. Kano, K., Suzuki, M. & Akatsuka, H. Spectroscopic measurement of electron temperature and density in argon plasmas based on collisional-radiative model. *Plasma Sources Sci. T.* **9**, 314–322. https://doi.org/10.1088/0963-0252/9/3/309 (2000).
49. Friedl, R. & Fantz, U. Spectral intensity of the N < sub > 2 emission in argon low-pressure arc discharges for lighting purposes. *New. J. Phys.* **14** https://doi.org/10.1088/1367-2630/14/4/043016 (2012).
50. Shimizu, T., Sakiyama, Y., Graves, D. B., Zimmermann, J. L. & Morfill, G. E. The dynamics of ozone generation and mode transition in air surface micro-discharge plasma at atmospheric pressure. *New. J. Phys.* **14** https://doi.org/10.1088/1367-2630/14/10/103028 (2012).
51. Yang, W. & Dong, Z. W. Electron-vibrational energy exchange in nitrogen-containing plasma: A comparison between an analytical approach and a kinetic model. *Plasma Sci. Technol.* **18** https://doi.org/10.1088/1009-0630/18/1/03 (2016).
52. Zhu, H. L., Huang, Q. X., Wu, Y. F., Li, Y. R. & Ren, K. C. Formation and destruction of striation plasmas in Helium glow discharge at medium pressures. *Plasma Sci. Technol.* **24**, 7. https://doi.org/10.1088/2058-6272/ac496d (2022).
53. Lisovskiy, V. A., Koval, V. A., Artushenko, E. P. & Yegorenkov, V. D. Validating the Goldstein-Wehner law for the stratified positive column of dc discharge in an undergraduate laboratory. *Eur. J. Phys.* **33**, 1537–1545. https://doi.org/10.1088/0143-0807/33/6/1537 (2012).
54. Pintassilgo, C. D. & Guerra, V. Modelling of the temporal evolution of the gas temperature in N_2 discharges. *Plasma Sources Sci. T.* **26**, 15. https://doi.org/10.1088/1361-6595/aa5db2 (2017).
55. Plessis, P., Marmet, P., & Dutil, R. Ionization and appearance potentials of ch4 by electron-impact. *J. Phys. B-At Mol. Opt. Phys.* **16**, 1283–1294. https://doi.org/10.1088/0022-3700/16/7/019 (1983).
56. Scharnweber, D., Schlottig, F., Oswald, S., Becker, K. & Worch, H. How is wettability of titanium surfaces influenced by their preparation and storage conditions? *J. Mater. Sci. -Mater Med.* **21**, 525–532. https://doi.org/10.1007/s10856-009-3908-9 (2010).
57. Susin, C. et al. Safety and efficacy of a novel, gradually anodized dental implant surface: A study in Yucatan mini pigs. *Clin. Implant Dent. Relat. Res.* **21**, 44–54. https://doi.org/10.1111/cid.12754 (2019).
58. Barbosa, T. P. et al. Topography and surface energy of dental implants: A methodological approach. *J. Braz Soc. Mech. Sci. Eng.* **39**, 1895–1907. https://doi.org/10.1007/s40430-016-0700-x (2017).
59. Wang, R. et al. Light-induced amphiphilic surfaces. *Nature* **388**, 431–432 (1997).
60. Liu, X., Hua, R., Niu, J., Zhang, Z. & Zhang, J. N2 plasma treatment TiO_2 nanosheets for enhanced visible light-driven photocatalysis. *J. Alloys Compd.* **881** https://doi.org/10.1016/j.jallcom.2021.160509 (2021).
61. Sattha, C., Sakulkalavek, A. & Sakdanuphab, R. in *2nd International Conference on Science and Technology of Emerging Materials (STEMa).*Amer Inst Physics, (2018).
62. Li, H., Belkind, A., Jansen, F. & Orban, Z. An in situ XPS study of oxygen plasma cleaning of aluminum surfaces. *Surf. Coat. Technol.* **92**, 171–177. https://doi.org/10.1016/s0257-8972(97)00079-0 (1997).
63. Kubies, D. et al. The interaction of osteoblasts with bone-implant materials: 1. The effect of physicochemical surface properties of implant materials. *Physiol. Res.* **60**, 95–111. https://doi.org/10.33549/physiolres.931882 (2011).
64. Le Guehennec, L. et al. Osteoblastic cell behaviour on different titanium implant surfaces. *Acta Biomater.* **4**, 535–543. https://doi.org/10.1016/j.actbio.2007.12.002 (2008).
65. Tominami, K. et al. Cold atmospheric plasma enhances osteoblast differentiation. *PloS One*. **12** https://doi.org/10.1371/journal.pone.0180507 (2017).
66. Gongadze, E. et al. Adhesion of osteoblasts to a nanorough titanium implant surface. *Int. J. Nanomed.* **6**, 1801–1816. https://doi.org/10.2147/ijn.S21755 (2011).
67. Anitua, E. et al. Influence of calcium ion-modified implant surfaces in protein adsorption and implant integration. *Int. J. Implant Dent.* **7** https://doi.org/10.1186/s40729-021-00314-1 (2021).

68. Pegueroles, M. et al. Effect of blasting treatment and fn coating on MG63 adhesion and differentiation on titanium: A gene expression study using real-time RT-PCR. *J. Mater. Sci. Mater. Med.* **22**, 617–627. https://doi.org/10.1007/s10856-011-4229-3 (2011).
69. Yang, Y. Z., Cavin, R. & Ong, J. L. Protein adsorption on titanium surfaces and their effect on osteoblast attachment. *J. Biomed. Mater. Res. A*. **67A**, 344–349. https://doi.org/10.1002/jbm.a.10578 (2003).
70. Kim, W. J. et al. Enhanced protein immobilization efficiency on a TiO_2 surface modified with a hydroxyl functional group. *Langmuir* **25**, 11692–11697. https://doi.org/10.1021/la901615e (2009).
71. Park, J. W. et al. Osteoblast response and osseointegration of a Ti-6Al-4V alloy implant incorporating strontium. *Acta Biomater.* **6**, 2843–2851. https://doi.org/10.1016/j.actbio.2010.01.017 (2010).
72. Maeno, S. et al. The effect of calcium ion concentration on osteoblast viability, proliferation and differentiation in monolayer and 3D culture. *Biomaterials* **26**, 4847–4855. https://doi.org/10.1016/j.biomaterials.2005.01.006 (2005).
73. Romero-Gavilán, F. et al. Protein adsorption/desorption dynamics on Ca-enriched titanium surfaces: Biological implications. *J. Biol. Inorg. Chem.* **26**, 715–726. https://doi.org/10.1007/s00775-021-01886-4 (2021).
74. Mesa-Restrepo, A. et al. Osteointegration of Ti bone implants: A study on how surface parameters control the foreign body response. *ACS Biomater. Sci. Eng.* **10**, 4662–4681. https://doi.org/10.1021/acsbiomaterials.4c00114 (2024).
75. Blank, M. & Sims, N. A. Cellular processes by which osteoblasts and osteocytes control bone mineral deposition and maturation revealed by stage-specific EphrinB2 knockdown. *Curr. Osteoporos. Rep.* **17**, 270–280. https://doi.org/10.1007/s11914-019-00524-y (2019).
76. Zhang, Y. Y. et al. Effect of microtopography on osseointegration of implantable biomaterials and its modification strategies. *Front. Bioeng. Biotechnol.* **10**, 14. https://doi.org/10.3389/fbioe.2022.981062 (2022).

Acknowledgements

This work was supported in part by the NRF Grant funded by the Korean Government (NRF-2022R1A2C2010940). This work was also supported by a KAIST grant (No. G04220008) funded by the Korean government, and by the Technological Innovation R&D Program (RS-2023-00275019) funded by the Ministry of SMEs and Startups (MSS, Korea).

Author contributions

Designed the studies: A.J., H.L., H.J.J., S.P., and B.G.; Performed the experiments: A.J., H.L., and H.K.; Analyzed the data: A.J., H.L., H.J.J., and H.K.; Wrote the manuscript: A.J., H.L., H.K., H.J.J., S.P., and B.G.; Supervised all studies: S.P. and B.G.; All authors critically reviewed the report and approved the final version.

Declarations

Competing interests

The authors declare no competing interests.

Additional information

Supplementary Information The online version contains supplementary material available at https://doi.org/10.1038/s41598-024-82730-y.

Correspondence and requests for materials should be addressed to S.P. or B.G.